Copyright ©2024 by the International Astronautical Federation (IAF). All rights reserved.

IAC-24,A6,6,4,x90969

Integrated GNC Design and Implementation for e.Inspector mission: multi-spectral imaging for spacecraft debris in preparation to active removal

Stefano Silvestrini[a], Andrea Colagrossi[a], Michele Bechini[a], Michele Ceresoli[a], Gaia Letizia Civardi[a], Lorenzo Capra[a], Michèle Lavagna[a], Robin Biesbroek[b]

[a] *Politecnico di Milano, Department of Aerospace Science and Technology, Milan, 20156, Italy*
[b] *ESA-ESTEC, Keplerlaan 1, 2201 AZ Noordwijk, The Netherlands*

Abstract

The miniaturization of space technology allows small satellites to perform in-orbit servicing missions, offering flexibility and cost reduction. However, autonomous proximity, berthing, and docking maneuvers must be tested and verified in orbit. The e.Inspector mission aims to fly around debris at 600 km altitude, reconstructing its shape and dynamics to prepare for capture. The GNC-IP system adjusts image acquisition based on target distance, detecting debris using VIS and TIR cameras. Relative navigation is achieved through a differential absolute filter, while Model Predictive Control (MPC) manages trajectory and control.

Keywords: guidance, navigation, control, mpc, optical navigation, multi-spectral

1. Introduction

The rapid space technology miniaturization opens the chance to perform In-Orbit servicing missions with small satellites, gaining in servicers agility, flexibility, time to market and cost reduction. However, still some crucial capabilities servicers shall ensure to perform autonomous proximity, berthing and docking maneuvering, have to be consolidated and on orbit verified. Among those, the target object to service
dynamics and actual shape reconstruction is of primary relevance. In fact, those information are prodromic to any further operation which entails the chaser-target contact. The e.Inspector mission, currently under phase B, is an ESA funded mission aimed at flyaround a debris – 600 km height flying - to precisely reconstruct the target shape and dynamics in preparation of its capture for removal.
The GNC-IP architecture features two main submodes depending on the distance from the selected target. In particular, the main difference is the image acquisition strategy and consequent processing. The proximity phases start after the absolute orbital transfer. The rationale behind the hand-over to relative navigation is to balance two functionalities:

- during absolute phase the target position is estimated only with provided TLE, carrying an uncertainity that can go up to few km.
- the relative navigation starts when a robust target detection can be performed.

When the target is only few pixels in the cameras FOV, namely at the initialization of the proximity phase, long exposure images are foreseen. Whereas, as soon as the target blob increases to few tenths of pixel the frame acquisition is static.

The VIS pipeline works as a blob detector using the invariance of the star illumination conditions against the illumination condition of the artificial target. It basically extracts the contours of light points in the image, calculates the convex hull closure and proposes a target detection based on the fact that the only outlier is the target, presumably. The advantage of such technique is that the detection is agnostic to the geometry of the target and thus can be applied to the target debris as well as any backup targets. The TIR feature detection resembles the centroid technique. Cross-reprojection of VIS-TIR detection is used as feature fusion and to derive indications on measurement uncertainty to be fed to the filter.

The relative navigation exploits the usage of a differential absolute filter, which estimates the absolute state of both the target and the chaser. The relative state is then retrieved by computing the difference between these two. Since such design introduces a coupling between the relative and the absolute navigation, a more robust alternative is to retrieve the state of the chaser from the output of the absolute OD module.

The main advantage of adopting this architecture is that it easily allows to introduce a much more accurate dynamical propagation model in the filter prediction step, since the estimated state is expressed in an inertial reference frame. In terms of measurements, the filter again receives the target Line of Sight (LOS) unit vector that is extracted from the VIS and TIR cameras, while Two Line Elements of the target are periodically uploaded from ground. To enhance the filter's robustness to faulty measurements an outlier rejection routine based on the Mahalanobis distance check is introduced.

Model Predictive Control (MPC) is selected as the baseline algorithm for the guidance and control implementation, to perform the transitions between the

Copyright ©2024 by the International Astronautical Federation (IAF). All rights reserved.

hold point/orbits and the drift orbits around the target. The transfer trajectories and the control input, in the form of an acceleration vector, are provided by the MPC controller which works optimally and effectively within the defined constraints and considering the interactions between system variables. The MPC implementation is based on a quadratic convex optimization with linear description of the dynamics, formulated via Relative Orbital Elements and including the J2 perturbation.

2. GNC Architecture

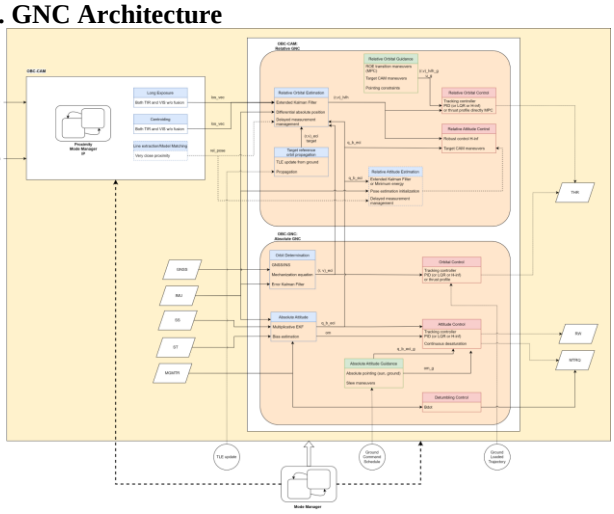

Figure 1: GNC algorithm scheme.

Figure 1 reports the high-level architecture of the GNC subsystem. The GNC can be divided into the absolute GNC module and the relative GNC module.

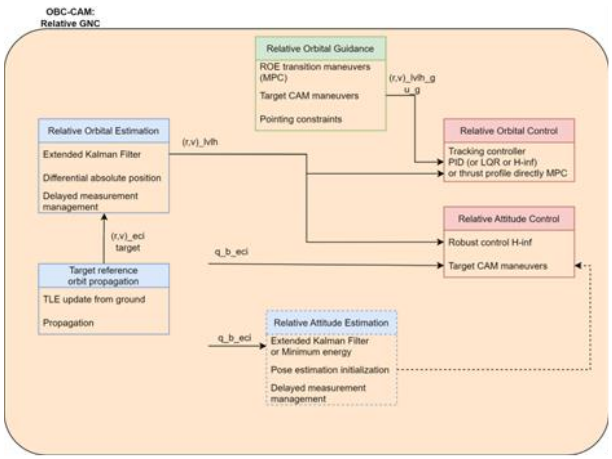

Figure 2: Relative GNC algorithm scheme.

Figure 2 shows the high-level architecture of the relative GNC module. The relative GNC takes input from the absolute attitude and orbit determination and from the on-board cameras. The output of the relative navigation filter is then fed to the Guidance and Control functional block. Even if present in the sketch, the relative attitude estimation, which is considered only a technology demonstrator, has not been implemented during the Phase-B of the project.

3. Processor in the Loop Validation

GNC-IP algorithms

The GNC-IP architecture features two main submodes depending on the distance from the selected target. In particular, the main difference is the image acquisition strategy and consequent processing. The proximity phases start after the absolute orbital transfer. The rationale behind the hand-over to relative navigation is to balance two functionalities:

1. during absolute phase the target position is estimated only with provided TLE, carrying an uncertainty that can go up to a few km.
2. the relative navigation starts when a robust target detection can be performed.

Hence, we want to be sure to start relative navigation as soon as possible given the uncertainty on the target location. Based on results of IP, this hold-point where the handover takes place can vary between 10-20 km, depending also on the selected target.

When the target is only few pixels in the cameras FOV, namely at the initialization of the proximity phase, long exposure images are foreseen. Whereas, as soon as the target blob increases to few tenths of pixel the frame acquisition is statis. In the following paragraphs the details on the algorithms are provided. To recall, the cameras FOV are reported here:

- 2048x2048 for the VIS imager
- 640x512 for the TIR imager
-

In both methods, the IP delivers two different LOS measurements which come from two independent pipelines. Nevertheless, since TIR detection is much easier due to the cancelling of the stars, the option of reprojecting the TIR measurement on the VIS has been kept as possible, either to deliver a validity flag or to increase the uncertainty associated to that measurement. Indeed, the filter uses an outlier rejection based on the Mahalanobis distance with respect to the estimated state distribution. No feature fusion is implemented and two independent measurements are fed to the filter in any case.

IP – Far range

In the far range sub mode, the target spans only a few pixels in the camera frame for both VIS and TIR cameras.

Copyright ©2024 by the International Astronautical Federation (IAF). All rights reserved.

Namely, for the payloads considered and a relative chaser-target distance of about 1km, the characteristic length of VESPA (i.e., its height) result to be about 15 pixels in TIR images and about 30 pixels in VIS ones.

The long exposure images have been investigated for those initial phases when the VESPA target does not span sufficient pixels for the contour detection to run. Another approach could be to use subsequent acquisition to derive LOS detection when the target is only few pixels. As soon as the target spans more than tenths of pixel the IP mode could switch to short exposure. The images were created using associated trajectories including the determination/control performance.

The two alternatives represent a viable solution bringing pros and cons for the scenario. In particular: long exposure images have found to be less computationally expensive with respect to cross-correlation of subsequent images to retrieve the target; moreover, long exposure do not require any need for attitude knowledge keeping measurements uncorrelated from attitude filter state, although this will be investigated for the next implementation phase also for long exposure technique. On the other hand, especially in the noisy target pointing, attitude determination is needed to properly control the attitude pointing; the noisy inertial is deemed to be less constraining in term of attitude control. If one puts the two methods in perspective, the rationale is the same. On one hand, with long exposure images sequence-dependent features are directly imaged by the cameras, on the other hand subsequent frame correlation tries to retrieve the same pattern with handcrafted algorithms.

To improve detectability with respect to the background (i.e., stars), it has been decided to operate the cameras in long exposure mode with an exposure time of 10 seconds. This value will be subjected to extensive test with hardware-in-the-loop and mock-up images in a representative environment. Within this context, two main scenarios are analysed, i.e., the "*noised inertial pointing*" and the "*noised target pointing*". The noised inertial pointing refers to the case in which the chaser points in a fixed inertial direction and detects space objects passing through the FOV of the cameras, while the noised inertial pointing is the case in which the chaser starts pointing in the direction in which the target is supposed to be and tracks this point through the propagation of the orbit. Both the scenarios are defined "*noised*" since uncertainties due to the pointing accuracy, chaser control inaccuracies, and possible discrepancies between the target actual position and its estimate from ground are considered when propagating the relative orbits. Namely, these disturbances have been quantified in a random displacement of 20m along the three axes of the current target position, a random gaussian noise on the chaser-to-target quaternion with a standard deviation of 0.05° and an uncertainty on the target velocity of 0.01m/s. The long exposure images are selected as the best imaging strategy for the LOS estimation since they allow distinguishing the target from the background in both the scenarios. Namely, in noisy target pointing, the target will appear in the image as a blob, while the stars will cast a wake due to the attitude dynamics of the chaser. On the contrary, in the noisy inertial pointing, the stars will be projected in the images as blobs, while the target will cast a wake due to its relative motion with respect to the chaser.

The synthetic images are generated in the absence of the Earth as background (since the analyses performed confirmed that the Earth is within the camera FOV only for the close inspection) and by assuming that the only target spacecraft that can be within the FOV is VESPA (despite the algorithm developed do not depend on the target's shape). Notice that the TIR sensor noise has been applied to the input TIR images, in a first approximation, by using the characteristic TIR noise sources and parameters outlined in [RD8]. The ADC Gain for the TIR noise model has been set to 12000 ADU/V (about four times the value in [RD8]) to obtain highly noised TIR images. It is acknowledged that this is just a first approximation and a better characterization of the TIR noise sources and the actual "long exposure" TIR image formation is forecasted as future development activity to enhance the representativeness of the synthetic TIR images. Figure 3 shows an example of a VIS noisy long exposure image (left) and its corresponding TIR noised version (right) in the noised inertial pointing scenario, while Figure 4 shows a VIS noised image and its corresponding TIR noised frame in the noised target pointing scenario.

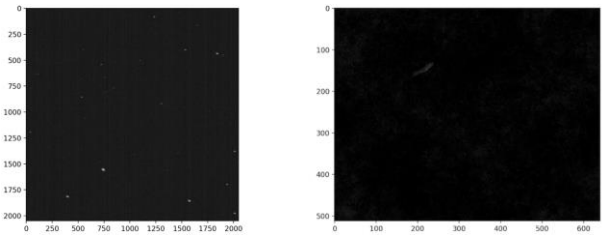

Figure 3: Examples of synthetic noised long exposure images (VIS left, TIR right) in noisy inertial pointing scenario.

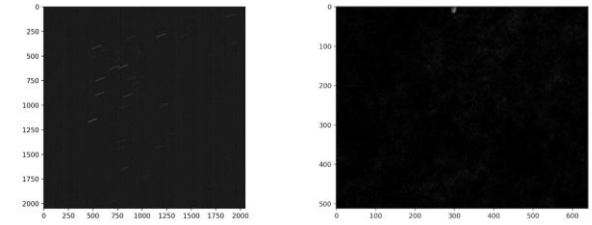

Figure 4: Examples of synthetic noised long exposure images (VIS left, TIR right) in noisy target pointing scenario.

Copyright ©2024 by the International Astronautical Federation (IAF). All rights reserved.

Noisy Target Pointing Scenario

A general overview of the algorithm developed for the target pointing scenario is shown in Figure 5.

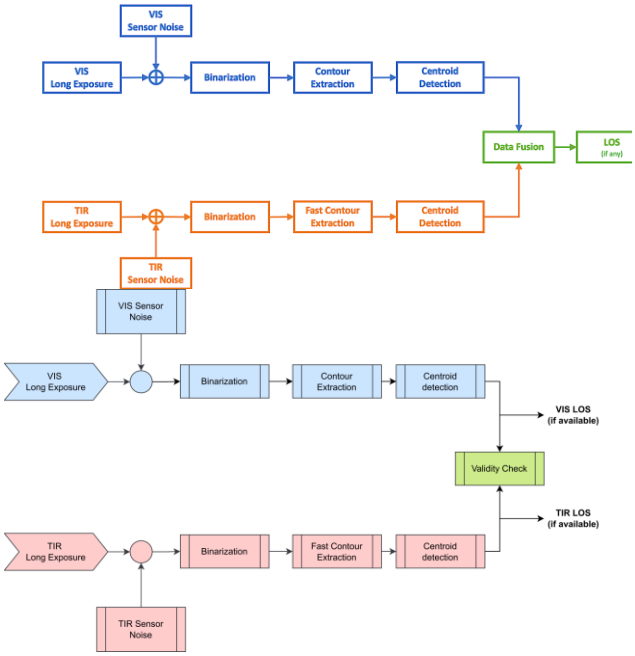

Figure 5: Noisy target pointing algorithm overview.

The algorithms compute two independent LOS from the TIR and the VIS images independently and then it fuses the information of the two streams returning a single LOS expressed in VIS reference frame and TIR reference frame. The two streams are almost equal and leverages the fact that if in each time the target is located almost always in the same pixels, or in a restricted area of the total pixel array, the intensity of those pixels will be higher with respect to the intensity of the pixels covered by the wake of the stars. This intuition comes from the fact that the photons received in 10 sec by the detector and coming from the target will be localized in a small number of pixels due to the pointing strategy, while the photons coming from the other objects in the scene (i.e., the stars) will be spread to form a wake. This holds true for TIR images (where the stars are not present) and for the VIS images in which the target is well illuminated. In such cases the position of the centre of the blob is detected by binarizing the image and subsequently extracting the most circular blob and computing its centre. In some cases, due to bad illumination conditions, the VIS images results in a more difficult detection that is handled by detailing more the blob detection steps through a more in-depth analyses of the contours extracted. Where to adopt the "fast" detection (i.e., single blob) or the more detailed one is automatically detected by the algorithm based on the confidence of the "fast" detection, i.e., if there are more than a single candidate contour that meet the criteria defined, a more detailed step will be needed. An example of the "fast" processing of VIS images with intermediate steps is shown in Figure 311, while Figure 6 shows the intermediate steps of the detailed processing of VIS images. The processing of TIR images with the intermediate steps is shown in Figure 7.

(a) Input noised grayscale image. **(b)** Binary image with noise removed. **(c)** Detected contour and computed centroid.

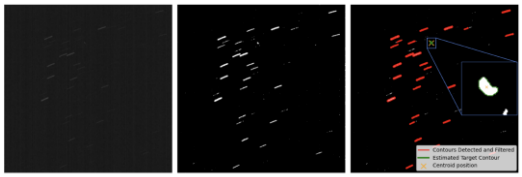

(a) Input noised grayscale image. **(b)** Thresholded binary image. **(c)** Detected contours and computed centroid.

Figure 6: Example of detailed processing of VIS images.

(a) Input noised grayscale image. **(b)** Thresholded binary image. **(c)** Detected contours and computed centroid.

Figure 7: Example of processing of TIR images.

The fusion of the VIS and TIR images is based on the reprojection of LOS-VIS into TIR FOV and vice versa. By checking the results of the reprojection, it is possible to detect false detection (e.g., due to the array size of the cameras, if the LOS-VIS is available and the LOS-TIR is not available, but the reprojected LOS_VIS in TIR is inside the FOV, it is likely to be a false detection). Validity flags are raised in case of umbiguous detections. Examples of the final retrieved LOS in VIS camera frame after the VIS-TIR sensors data fusion step is shown in Figure 8.

Copyright ©2024 by the International Astronautical Federation (IAF). All rights reserved.

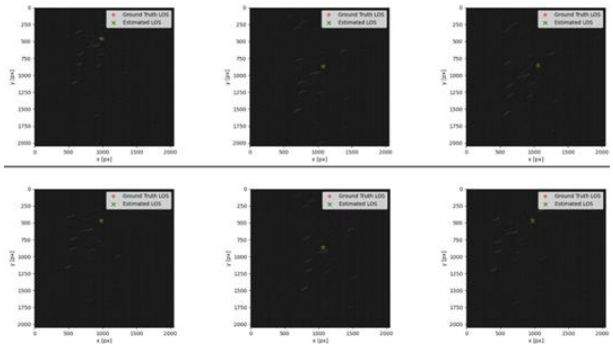

Figure 8: Examples of LOS detections in Noisy Target Pointing

The algorithm has been tested by using noised VIS and TIR images (namely 600 with target in FOV and 600 with target not in FOV) with a relative distance of about 1km. Notice that, as outlined above, due to differences in the FOVs, the target may be detectable by the VIS, but not by the TIR. The confusion matrix retrieved from the outcomes on the test set leveraging the VIS-TIR sensors data fusion is shown in Figure 9. Notice that for the current dataset, the ground truth true positives are equal to the ground truth true negatives, i.e., both equal to 600 samples. The algorithm is highly robust in detecting if the target is within the VIS FOV, with 597 true negatives out of 600 and only one false negative. Notice that LOS detection with an error between the detected target position in pixels and its ground truth value higher than 22 pixels have been classified as False Positives (i.e., wrong detections). The algorithm proposed is quite accurate, with 527 true positives and 75 false positives. Notice that 72 of the false positives (i.e., 96%) are classified as false positives due to the tolerance imposed on the Euclidean distance between estimated and ground truth LOSs, while a LOS has been detected even if the target was not within the FOV for only 3 images.

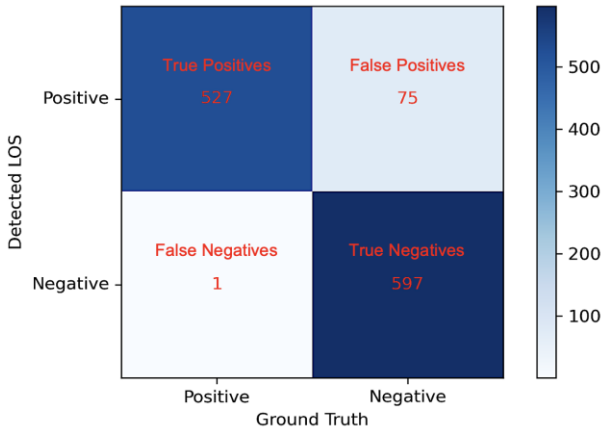

Figure 9: LOS detection confusion matrix in noised target pointing scenario.

The scores in terms of Precision, Recall, and F1-score are provided in Table 1, highlighting that the algorithm well balances the trade-off between precision and recall, with a very high rate of correct detection of the presence of target within the FOV with a good precision score.

Table 1: LOS detection metrics in Noisy Target Pointing long exposure.

Metric	Value
Precision	0.875
Recall	0.998
F-1	0.933

The angular error distribution for the True Positive LOS vector estimates is shown in Figure 10. The mean angular error is 0.053 degrees with a standard deviation of 0.025 degrees due to a mean LOS distance error in the image reference frame of 11.70 pixels with a standard deviation of 5.55 pixels.

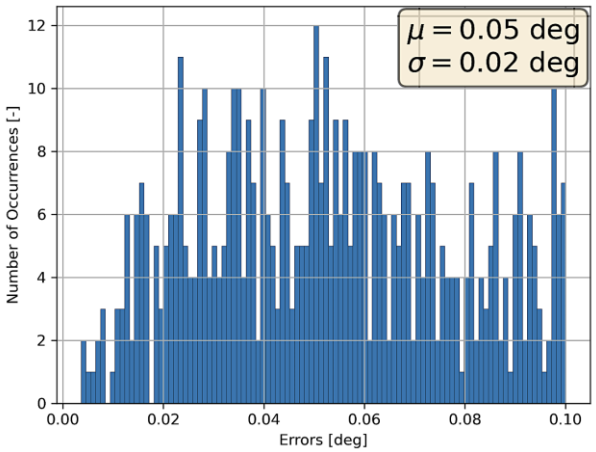

Figure 10: LOS angular error distribution in noised target pointing scenario.

The computational times reported in Figure 11 are computed on an Apple® Silicon™ M1 Pro, using CPU only. The mean computational time to process the VIS images is 23.67 ms on average. The histogram of the VIS image processing computational time highlights two regions, one at about 8–10ms, and the other between 30ms to 60ms. This split is due to the fast processing of the VIS images that leads to a LOS estimation in a reduced amount of time for almost 400 images. Instead, when the fast processing fails, the needed more detailed analyses at least double the computational time. Please notice that the highest variability in the computational time in case the detailed image processing is needed is due to the number of thresholding iterations needed to achieve the mean intensity threshold and to the number

Copyright ©2024 by the International Astronautical Federation (IAF). All rights reserved.

of contours extracted that need to be processed. Concerning the TIR image processing, the simplified algorithm adopted allows achieving a computational time of about 1.47 ms, while the VIS-TIR sensors data fusion step has an almost null contribution to the overall computational time since it lasts in about 0.12 ms on average. The very preliminary results for the IP execution times were used as rough order of magnitude during the algorithm development. Nevertheless, quantitative results on the representative Q8 board have been reported in the PIL section, where roughly the conversion factor is ~10.

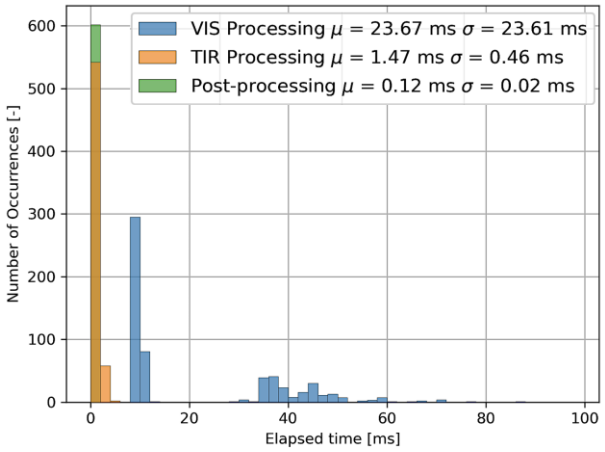

Figure 11: Computational time on CPU for the LOS estimation algorithm in noised target pointing scenario.

Noisy Inertial Pointing Scenario

A general overview of the algorithm developed for the Noisy Inertial Pointing Scenario is shown in Figure 12.

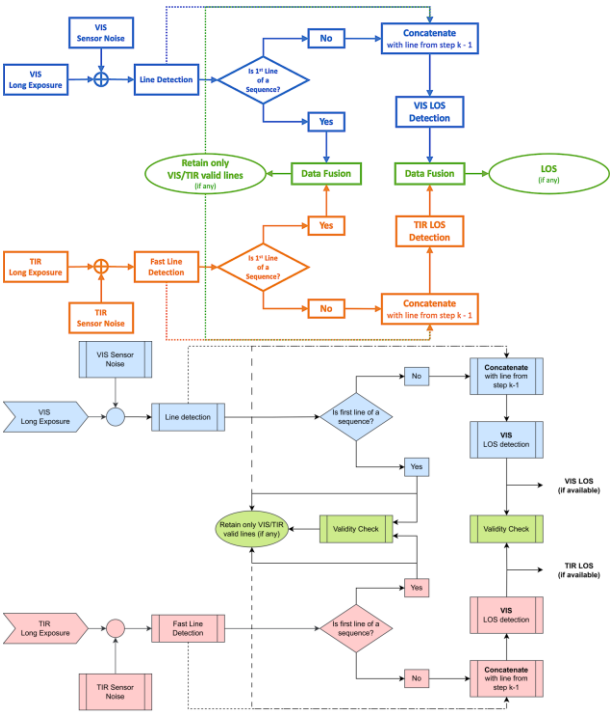

Figure 12: Noisy Inertial Pointing algorithm overview.

The algorithm developed for the noised inertial pointing scenario leverages the different shapes that the target and background stars (present only in the VIS images) assume in the long exposure images. As previously outlined, the target casts a wake due to the relative motion with respect to the chaser, while the stars appear as blobs. Hence, the algorithm implemented leverages a line detection step in which the wake belonging to the target is detected and approximated as a single line segment in both the images. Namely, the target wake is detected through a fast line segment detector named ELSED [RD10]. Then, to solve the ambiguity in selecting which of the two ends of the line corresponds to the current target position, the subsequent image is processed to extract another line. The two lines are then concatenated and the current target position (i.e., the LOS) can be detected from the second image and for all the subsequent images for which a line is detected and concatenated with the line estimated in the previous image by noticing that the target position in the second image corresponds to the line segment endpoint not matched during the concatenation. The same procedure is applied both to the VIS and the TIR images and the sensor fusion is exploited both to increase the robustness of the first line detected (the one for which the LOS is not estimated due to the ambiguity) by comparing the line retrieved from the two images through a reprojection of the TIR line in the VIS image, and to increase the robustness of the final LOS retrieved by comparing the VIS and TIR LOS estimates by relying on the VIS-to-TIR and/or TIR-to-VIS reprojection of the LOS estimates. Notice that, due to the high noise and

Copyright ©2024 by the International Astronautical Federation (IAF). All rights reserved.

disturbance content of the VIS images rather than the TIR ones, the VIS images undergoes to a pre-processing step aimed at increasing the contrast of the wake with respect to the background (leveraging a customized histogram equalization and blurring scheme) and removing the strongest disturbances (i.e., the residual noise blobs and the brightest stars), easing the line detection step at the cost of a more computationally demanding process with respect to the processing time of TIR images. An example of the processing of VIS images with intermediate steps is shown in Figure 13, while Figure 14 shows the intermediate steps of the processing of TIR images.

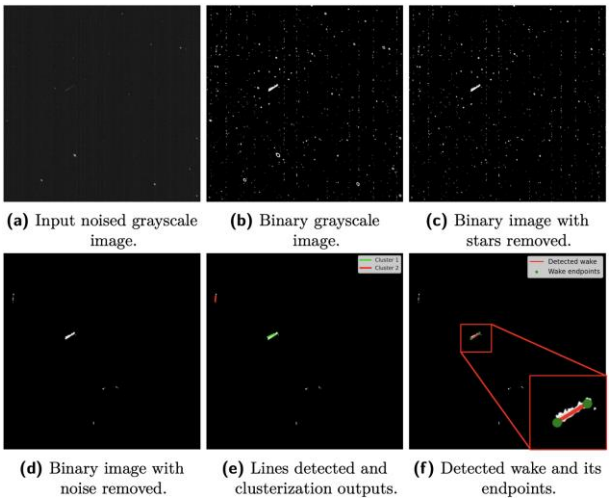

Figure 13: Example of processing of VIS images.

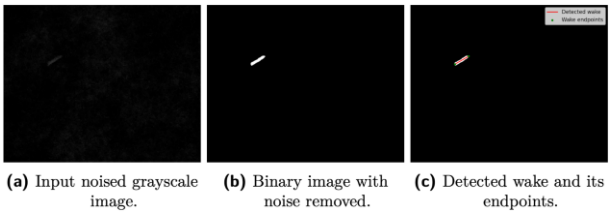

Figure 14: Example of processing of TIR images.

The data fusion of the wakes retrieved by the line detection step in VIS and TIR images is performed if at least one of the processed images between the TIR and the VIS at the current step is the first of a sequence. Notice that due to failure of the algorithm or due to a target visible only in one of the two images (the TIR has a reduced array size and FOV hence, the target can be visible only in VIS images, while, if the target is in shadow, it can be visible only in TIR images), the image processed can be the first of a sequence in one of the two streams but not in the other. The LOS estimation within a stream is performed if the sequencing for the current stream has already been triggered by the line checks discussed above. The steps adopted to detect the LOS from two subsequent images are the same for the TIR and the VIS images. Notice that two subsequent wakes detected in successive images acquired by maintaining a fixed pointing direction shall have a common point (i.e., the end of the first wake and the start of the subsequent one) in an ideal scenario, with no time delays and a shutter instantaneously opening and closing. Hence, the wakes detected in two sequenced images (k and k − 1) are processed to identify the current LOS candidate, i.e., the endpoint of the wake k furthest to the endpoints of the wake k − 1. The LOS data fusion steps compare the LOS in the image reference frame obtained from VIS and TIR images to validate the outcomes similarly to the case of noisy target pointing. Validity flags are raised but, if present, two distinct measurements are issued. Examples of the final retrieved LOS in VIS camera frame after the VIS-TIR sensors data fusion step is shown in Figure 15. Please notice that the LOS is not available for the 1st image of a sequence due to the ambiguity of the two endpoints of the detected wake.

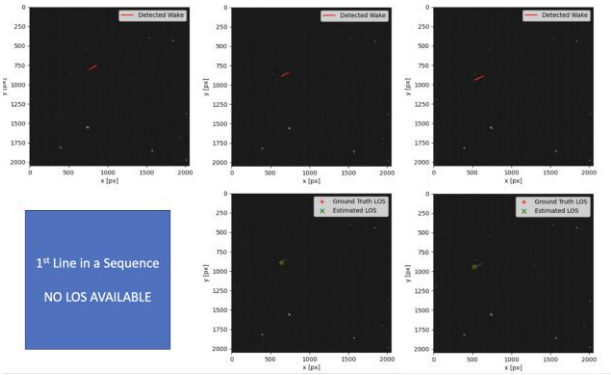

Figure 15: Examples of wake detection and LOS extraction after VIS-TIR data fusion step.

The algorithm has been tested by using noised VIS and TIR images (namely 300 with target in FOV and 300 with target not in FOV) with a relative distance of about 1km. Notice that, as outlined above, due to differences in the FOVs, the target may be detectable by the VIS, but not by the TIR. The main metric adopted to evaluate the outcomes of the implemented algorithm is the LOS angular error eLOS, $\theta eLOS$, θ already adopted also for the case of noised target pointing.

The confusion matrix retrieved from the outcomes on the test set leveraging the VIS-TIR sensors data fusion is shown in Figure 16. Notice that, similarly to the case of noised target pointing, a LOS detected is considered as a False Positive if the error with respect to the ground truth target position in image frame is higher than 22 pixels.

Copyright ©2024 by the International Astronautical Federation (IAF). All rights reserved.

Notice that the true negatives are 348 because there are 300 images with target not in FOV and 48 images for which the LOS cannot be retrieved since they are the first images of their sequence. The algorithm is highly robust in detecting if the image contains the target, resulting in 348 true negatives and 0 false negatives. Also in this case, the algorithm is highly precise and accurate in determining if the target is within the FOV, resulting in only 3 false positives. Notably, the highest distance between the detected and the ground truth LOS is about 25 pixels.

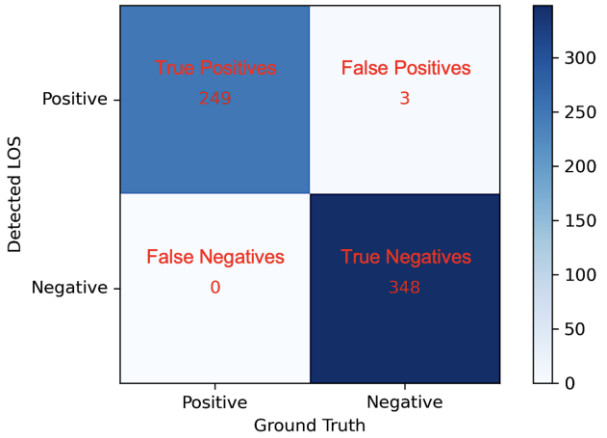

Figure 16: LOS detection confusion matrix in noised inertial pointing scenario.

The precision, recall, and F1-score have been computed to evaluate quantitatively the performances and reported in Table 2, resulting in being highly precise and robust with an optimal balance between precision and recall.

Table 2: LOS detection metrics in Noisy Inertial Pointing long exposure

Metric	Value
Precision	0.988
Recall	1.0
F-1	0.994

The angular error distribution for the True Positives detected is shown in Figure 17. Notably, the algorithm achieved a mean angular error of 0.034 degrees with a standard deviation of 0.020 degrees. In terms of distance error in the image reference frame, the algorithm achieved a mean error of 7.55 pixels with a standard variation of 4.53 pixels.

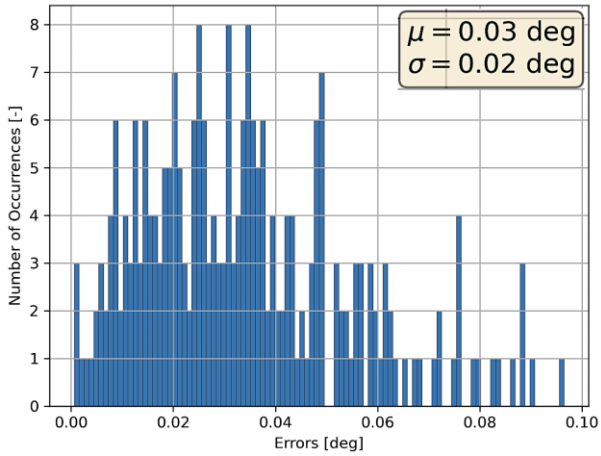

Figure 17: LOS angular error distribution in noised inertial pointing scenario.

The computational times reported in Figure 18 are computed on an Apple® Silicon™ M1 Pro, using CPU only. the computational time required to process the VIS images is about 169 ms and it is the highest within the algorithm due to the image processing steps needed to enhance the contrast and remove the various noises in the binarized image. Notably, the mean processing time for a TIR image is about 2.98 ms due to the simple image processing steps needed to retrieve a LOS. Finally, the sensor data fusion validity check steps performed have an almost null impact on the overall computational time (that on average is about 172 ms), since the mean time required for this step is in the order of 0.1 ms. The very preliminary results for the IP execution times were used as rough order of magnitude during the algorithm development. Nevertheless, quantitative results on the representative Q8 board have been reported in the PIL section, where roughly the conversion factor is ~10.

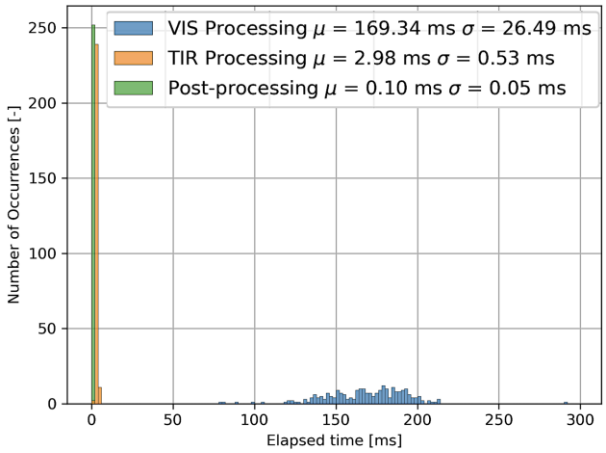

Figure 18: Computational time on CPU for the LOS estimation algorithm in noised inertial pointing scenario.

The signed error distribution is reported below:

Copyright ©2024 by the International Astronautical Federation (IAF). All rights reserved.

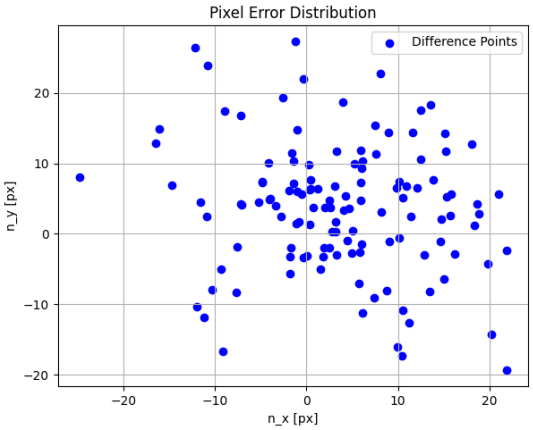

Figure 19: Signed error distribution

IP – Close range

In the close-range submode, the target spans at least few tenths of pixels in the camera frame for both TIR and VIS cameras. The acquisition rate of the camera is taken as 0.1 Hz, conservatively to acquire and process both images. Such frequency will be subject to extensive test with hardware in the loop.

A general overview of the algorithm is shown in Figure 20.

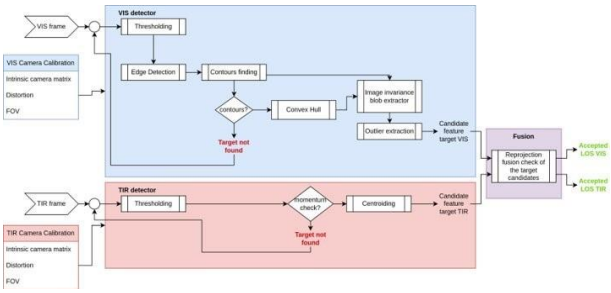

Figure 20: Close range image processing algorithm.

The image processing module computes two independent detections for the VIS and TIR image and fuse the information at the detection feature level.

The VIS pipeline works as a blob detector using the invariance of the star illumination conditions against the illumination condition of the artificial target. It basically extracts the contours of light points in the image, calculates the convex hull closure and proposes a target detection based on the fact that the only outlier is the target, presumably. The advantage of such technique is that the detection is agnostic to the geometry of the target and thus can be applied to Vespa as well as any backup targets.

An example of intermediate results is shown in figure in Figure 21.

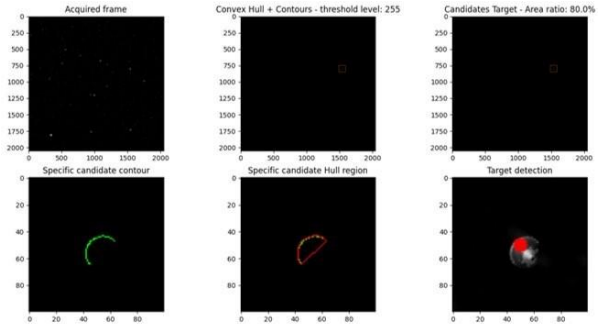

Figure 21: Blob detection intermediate results.

The TIR pipeline exploits a simpler centroid detection given that stars are not imaged, or much fainter, in the relevant spectrum.

The TIR and VIS detections are fused together by cross-reprojection to calculate the error distribution to be fed to the filter for each LOS measurement. An example is shown in Figure 22.

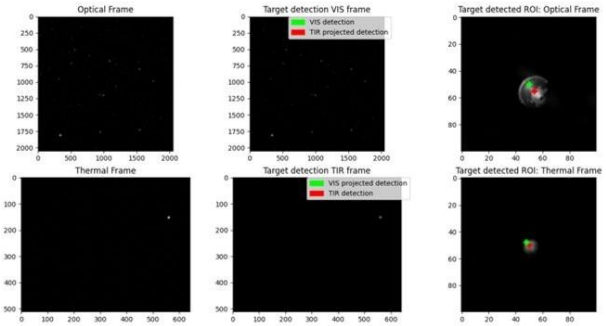

Figure 22: Cross-reprojection TIR and VIS fusion.

The close range has been tested for distances ranging IO#1-2-3-4 and HO#3-4. The target is generally visible in a ROI of at least 50 px.

- The dataset used for testing is randomly acquiring images of the target. The target may not be inside the FOV either or it may be visible only by the VIS camera, due to larger FOV. Few examples images are shown in Figure 22:

Copyright ©2024 by the International Astronautical Federation (IAF). All rights reserved.

Figure 23: Dataset images for close proximity acquisition.

- Derive metrics (Precision, Recall, F1) to correctly build performance model and evaluate accuracy performance

The results are shown collectively in Table 3:

- Assuming a TP detection if the error with respect to the groundtruth is less than 10 px, the metrics can be summarized as follows:

Table 3: Close proximity IP performance.

Metric	Value
Precision	0.82
Recall	0.96
F-1	0.88

- When a TP detection is performed the mean accuracy ranges with the distribution shown in the figure below (up right image) corresponding to ~0.5 px, ceiled to 1 px.
- The computational times are calculated using a 12th Gen Intel(R) Core (TM) i7-12700H – 4.7 GHz peak. Such values are used here solely for relative comparison between different alternatives. The very preliminary results for the IP execution times were used as rough order of magnitude during the algorithm development. Nevertheless, quantitative results on the representative Q8 board have been reported in the PIL section, where roughly the conversion factor is ~10.

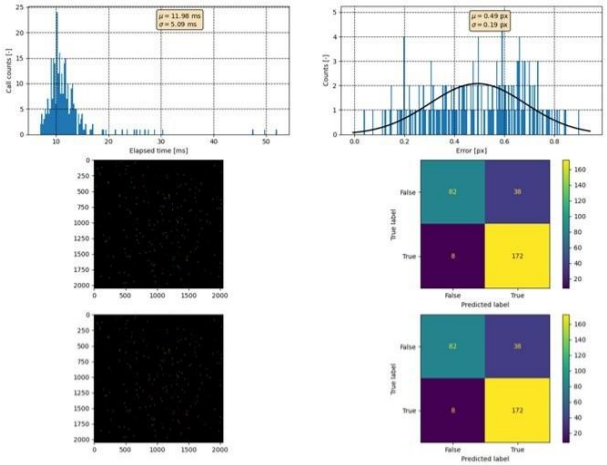

Figure 24: Close proximity IP algorithm performance indexes.

Images with detections are reported here to show the discrepancy with the groundtruth. As expected, being the algorithm sensitive to the illumination conditions, the error distribution is centered on the center of brightness in the two spectra. This is an additional reason to actually exploit TIR detection to check the LOS validity, even though not interfering with the distinct LOS output. In addition, the error distribution for the closest inspection (where the target spans several pixels) is reported below:

Copyright ©2024 by the International Astronautical Federation (IAF). All rights reserved.

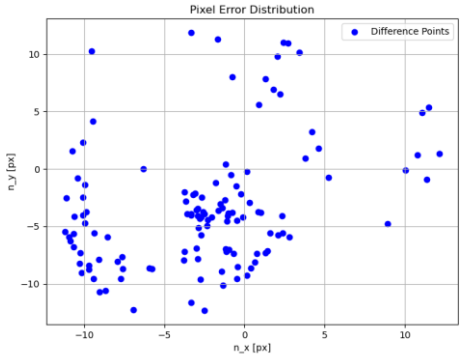

Figure 25: Signed error distribution

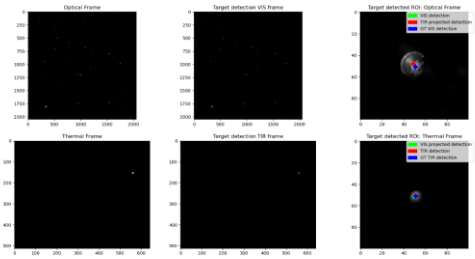

Figure 26: Example detection

6 Conclusion & Future Developments

The conclusions drawn from this study underscore the effectiveness of the image processing algorithm in detecting and tracking space debris in real-time, leveraging both optical and infrared cameras. The comprehensive testing methodology, which includes both Processor-in-the-Loop (PIL) and Hardware-in-the-Loop (HIL) phases, confirms that the algorithm is not only functional but also efficient in various environmental conditions.

The successful implementation of the algorithm on the Xiphos Q8 processor demonstrates the capability of high-speed processing necessary for real-time debris monitoring, critical for space missions aiming to capture and remove debris. The flexibility of the detection strategy—adapted for different proximity submodes—ensures that the system can operate effectively at various distances from the debris, from long-range detection with minimal pixels in the field of view to close-range, high-precision tracking.

Moreover, the fusion of data from the VIS and TIR cameras enhances the robustness of detection, allowing for reliable identification of debris in both long and short exposure images. The agnostic nature of the detection algorithm with respect to the target geometry adds further versatility, making it applicable for a wide range of debris shapes and sizes. The results indicate that this system is well-suited for the operational demands of future space debris removal missions, contributing significantly to mitigating the risks posed by space debris.

References

[1] M. Bechini, M. Lavagna, and P. Lunghi, “Dataset generation and validation for spacecraft pose estimation via monocular images processing”, Acta Astronautica, vol. 204, pp. 358–369, 2023, issn: 0094-5765. doi: 10.1016/j.actaastro.2023.01.012.

[2] M. Quirino, L. Marocco, M. Guilizzoni, M. Lavagna, High Energy Rapid Modular Ensemble of Satellites Payload Thermal Analysis Using OpenFOAM, Journal of Thermophysics and Heat Transfer (Mar.486,2021). doi:10.2514/1.T6165.

[3] M. Quirino, G. Sciarrone, R. Piazzolla, F. Fuschino, Y. Evangelista, G. Morgante, M. Guilizzoni, L. Marocco, S. Silvestrini, F. Fiore, M. Lavagna, HERMES CubeSat Payload Thermal Balance Test and Comparison with Finite Volume Thermal Model, Applied Sciences. doi:10.3390/app13095452.

[4] Quirino, M. and Lavagna, M., Thermal Image Generation Tool for Spacecraft Relative Navigation in Proximity Maneouvering Phases, Aerospace Europe Conference 2023 - Joint 10th EUCASS - 9th CEAS Conference, 10.13009/EUCASS2023-751

[5] J.R. Carpenter and C.N. D’Souza, Navigation Filter Best Practices. NASA Technical Report, 2018.

[6] T.D Larsen, N.A. Nils, R.O. Poulsen and N. Kjølstad, “Incorporation of Time Delayed Measurements in a Discrete-time Kalman Filter”. Proceedings of the 37th IEEE Conference on Decision and Control, 1998

[7] M. Bechini, “Monocular Vision for Uncooperative Targets through AI-Based Methods and Sensors Fusion”, PhD Dissertation, Politecnico di Milano, 2024

[8] L. Bianchi, “Synthetic Thermal Image Generation Towards Enhanced Close-Proximity Navigation in Space”, MSc Thesis, Politecnico di Milano, 2023

[9] European Machine Vision Association, “EMVA 1288 Standard: Standard for Characterization of Image Sensors and Cameras”, EMVA, Tech. Rep. Release 4.0 Linear, 2021.

[10] I. Suárez, J. M. Buenaposada, and L. Baumela, “Elsed: Enhanced line segment drawing”, Pattern Recognition, vol. 127, p. 108 619, 2022, issn: 0031-3203. doi: 10.1016/j.patcog.2022.108619.

[11] M. Quirino, “Novel thermal images generator for autonomous space proximity Operations”, Phd dissertation, Politecnico di Milano, 2023.

[12] NASA/Godda Space Flight Center Scientific Visualization Studio, Gaia dr2: Esa/gaia/dpac, Constellation figures based on those developed for the IAU by Alan MacRobert of Sky and Telescope magazine (Roger Sinnott and Rick Fienberg), 2018.

[13] T. Floherer, H. Krag, H. Klinkrad, “Assessment and Categorization of TLE Orbit Errors for the US SSN Catalogue”, 2008

Copyright ©2024 by the International Astronautical Federation (IAF). All rights reserved.

[14] G. Chang, “Robust Kalman filtering based on Mahalanobis distance as outlier judging criterion”, Journal of Geodesy, 2014

[15] E. Belloni, S. Silvestrini, J. Prinetto, M. Lavagna, “Relative and absolute on-board optimal formation acquisition and keeping for scientific activities in high-drag low-orbit environment”, Advances in Space Research, 2023.